

Resolvent analysis of high Reynolds number turbulent boundary layers subjected to pressure gradient histories

By T. Preskett[†], P. Jaiswal[†], B. Ganapathisubramani[†],
T. Jaroslowski, S. R. Gomez, S. Vijay, AND B. J. McKeon

To quantify the relative importance of the history effects on turbulent boundary layer (TBL) flows subjected to a streamwise-pressure gradient, a series of wind tunnel experiments, including hot-wire anemometry (HWA), oil-film interferometry (OFI), and particle image velocimetry (PIV) measurements at a high Reynolds number, $Re_\tau \approx 6000$, were carried out at the University of Southampton. The energetic large-scale structures in the flow are predicted from the mean flow through resolvent analysis, using only the mean velocity field as input. In particular, the biglobal resolvent analysis is used to account for the nonparallel effects encountered in the presence of a pressure gradient history, while a local resolvent analysis is performed at a downstream location where the local pressure gradient is near zero. A rank-1 amplification of the resolvent modes captures the shape of the turbulent kinetic energy spectrum and thus accounts for pressure gradient and history effects on large-scale structures. The framework shows that for flows that experience an adverse pressure gradient (APG), differences in mean shear upstream lead to the amplification of large-scale motions in the outer region of the boundary layer further downstream. However, some differences are observed between the amplified scales in the experimental measurements and resolvent analysis, and their exploration will be the subject of future studies.

1. Introduction

It is important to understand the role of mean pressure gradient histories on coherent structures of flow, as these structures are responsible for low-frequency fluctuations in wall shear stress and pressure that lead to noise and vibrations in a variety of applications (see Blake 2012, for instance). The relative balance between the local mean pressure gradient effect (dP/dx) and the local viscous effect (τ_w/δ^* , where τ_w is the local mean wall shear stress and δ^* is the local displacement thickness) is captured using Clauser's parameter, $\beta = (\delta^*/\tau_w)(dP/dx)$, where a high value of β suggests that the pressure gradient effects dominate over the shear stress at the wall. Previous studies typically focused on flows with nearly constant pressure gradient effects (i.e., typically constant β including zero) where an adverse pressure gradient (APG, $\beta > 0$) is known to increase the momentum deficit in the wake region in comparison to a zero-pressure gradient (ZPG, $\beta \approx 0$) TBL Aubertine & Eaton 2005) and decrease the extent of the log region in the outer flow (Harun *et al.* 2011). Meanwhile, a favorable pressure gradient (FPG; $\beta < 0$) suppresses the wake flow and extends the log region.

Some works have studied history effects where the boundary layer experiences a streamwise evolving pressure gradient. For example, Bobke *et al.* (2017) compared flows with

[†] Department of Aeronautics and Astronautics, University of Southampton, UK

different histories attaining near-constant values of β over large streamwise regions, finding that the turbulent statistics were sensitive to the upstream pressure gradient history. This is because the extent of turbulence amplification or attenuation depends on how different scales of motion respond to the imposed pressure gradient (Harun *et al.* 2011; Bobke *et al.* 2017; Volino 2020; Vishwanathan *et al.* 2023). The APG is known to amplify large scales and attenuate smaller scales, whereas FPG attenuates across all scales. The most prominent impact of the pressure gradient is on large- and very-large-scale motions (VLSMs) (Hutchins & Marusic 2007) that manifest as elongated, meandering streaks of low and high streamwise momentum that modulate the small-scale velocity fluctuations near the wall, shear stress, and pressure (Hutchins & Marusic 2007; Harun *et al.* 2013). Therefore, the change in turbulence statistics is directly related to the way in which the APG and FPG directly modify these large-scale structures, such as by altering their length, spacing, and spatial coherence (Volino 2020) or indirectly by altering the small scales through their modulation effects.

Note that large-scale structures become more prevalent and energetic with increasing Reynolds number, while the pressure gradient (especially the APG) includes its own footprint on the energetic structures. Therefore, it is important to decouple the effects of the pressure gradient history from those of changing Reynolds numbers. Recent work with sufficiently high APGs at low Reynolds numbers has shown that the turbulent kinetic energy shows a secondary peak in the outer layer (Sanmiguel Vila *et al.* 2020). However, the separation between the VLSM and the pressure gradient peak in this study was not clear due to the lack of sufficient scale separation. Sanmiguel Vila *et al.* (2020) also showed that small- and large-scale energy are modulated in the presence of APGs, and the location of the peak appears to be a function of both the Reynolds number and the pressure gradient. The mechanism driving the amplification of the large scale is unclear, and studies with a high Reynolds number with varying pressure gradient histories are needed.

A critical challenge in understanding the underlying flow mechanisms behind some of the above observations is that this is a multiscale flow problem. We need reduced-order models that can be used to explain and understand the role of inputs and their outputs. For instance, it would be useful to understand the causes of selective amplification in the outer layer under APGs and its role in the appearance of an additional spectral peak in streamwise velocity fluctuations. It would also be important to understand the same mechanisms behind the strengthening of VLSMs at high Reynolds numbers. Previous work on the resolvent analysis of turbulent channel flow (McKeon & Sharma 2010) has shown that reduced-order models based only on mean flow are capable of identifying the triadic interactions that are responsible for the generation or sustenance of flow structure. The resolvent analysis provides an orthonormal basis that is ordered by the singular values of the Resolvent operator, indicating the linear gain of the transfer function relative to a selected inner product. In the spectral domain for incompressible channel flows, areas with high turbulent kinetic energy coincide with regions where the resolvent operator is low rank (Moarref *et al.* 2013), suggesting that a small number of resolvent modes can represent energetic turbulent structures. Very recently, Gomez (2024) applied a biglobal resolvent approach to APG boundary layers with mean flow data obtained from direct numerical simulation/large-eddy simulation data. They found that an outer peak in streamwise velocity fluctuations can be identified in this manner. However, it is unclear whether this peak is related to the history of the pressure gradient or the emergence of VLSMs.

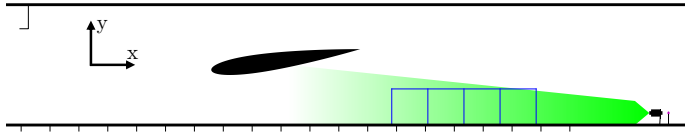


Figure 1: Sketch of the experimental setup for PIV and mean-static pressure measurements, shown in black solid lines. The laser optics and laser sheet are placed $20 \times \delta_{99}$ downstream of the measurements planes, shown as boxes.

This study uses, high Reynolds number experimental data collected in the boundary layer wind tunnel, where the scale separation allows one to distinguish various competing effects and pressure gradient histories. The remainder of this report is structured as follows. In Section 2, the resolvent framework and the experimental setup are briefly described. The results are discussed in Section 3, and conclusions are drawn in Section 4.

2. Methodology

2.1. Experimental setup

Experiments were carried out in the 12 m boundary layer wind tunnel at the University of Southampton. The tunnel has a cross section of $1.2 \text{ m} \times 1 \text{ m}$ (W×H). The flow was tripped at the inlet. This study required different pressure gradient histories to change the development in the boundary layer, which was done using NACA0012 airfoil with a chord length of 1.25 m mounted to the tunnel roof with four actuators that allowed its position to be varied. The quarter chord was kept at 0.5 m from the tunnel floor, and the angle of attack varied from -8° to 8° in steps of 4° . The inlet velocity was measured from a Pitot tube mounted one chord length upstream of the airfoil's leading edge, located 5.28 m from the tunnel inlet.

PIV measurements were performed at four different positions, using four LaVision Imager UX 25 MP cameras, as shown in Figure 1, with a magnification of ~ 17 pixels/mm. After processing, the fields of view from the 16 cameras were stitched together to create an area that measures approximately $26 \times \delta_{99}$, which is significantly larger than the boundary layer thickness and at least four times the size of the VLSMs. As such, the impact of the pressure gradient could be assessed across all scales, from large-scale motions to VLSMs.

Pressure taps were installed on the wind tunnel floor to measure wall pressure. For the smooth wall, 20 tubes with an inner diameter of 0.6 mm were fitted to the floor and spaced 0.245 m apart. Based on the results obtained from the panel method simulations, pressure taps were mounted to one chord upstream and downstream of the airfoil. OFI measurements were performed to measure wall-shear stress. OFI provides accurate estimates of the skin friction coefficient, with an uncertainty of $\pm 2\%$ (Tanner & Blows 1976).

2.2. Resolvent analysis

Here, terms are non-dimensionalized by the local friction velocity, u_τ , edge velocity, U_e , viscous length scale, ℓ_ν , and boundary layer thickness, δ_{99} , at the hot-wire location, which defines the Reynolds numbers $Re = \delta_{99}U_e/\nu$ and $Re_\tau = \delta_{99}/\ell_\nu$. The Navier-Stokes equations linearized about the temporally averaged mean flow field, $\mathbf{U}(\mathbf{x}_n)$, where \mathbf{x}_n

denotes the inhomogenous directions. The linearized Navier-Stokes equations are then Fourier transformed in time and in the statistically homogeneous directions, \mathbf{x}_h , as

$$\begin{aligned} -i\omega\hat{\mathbf{u}} + (\nabla\hat{\mathbf{u}})\mathbf{U} + (\nabla\mathbf{U})\hat{\mathbf{u}} - \frac{1}{Re}\nabla^2\hat{\mathbf{u}} + \nabla\hat{p} &= \hat{\mathbf{f}}_{\mathbf{u}}, \\ \nabla \cdot \hat{\mathbf{u}} &= 0, \end{aligned} \quad (2.1)$$

where the nonlinear terms have been replaced by an uncorrelated body force $\hat{\mathbf{f}}_{\mathbf{u}}$ following McKeon & Sharma (2010), and terms with hats are defined as Fourier modes

$$\hat{g}(\mathbf{x}_n) = \int \int g e^{i(\omega t - \mathbf{k} \cdot \mathbf{x}_n)} dt d\mathbf{x}_n, \quad (2.2)$$

with \mathbf{k} denoting the wavenumber vector and ω the temporal frequency. The no-slip boundary conditions at the wall are enforced.

In this study, we consider the local, parallel assumption where $\mathbf{x}_h = (x, z)$ and the modes are parameterized by (ω, k_x, k_z) , as well as the biglobal assumption such that $\mathbf{x}_h = (z)$ and the modes are parameterized by (ω, k_z) . In the former, the flow is assumed to vary slowly in x such that the only direction of variation is y and it neglects the nonparallel components of \mathbf{U} , while the latter incorporates the streamwise evolution in the mean flow field and x is chosen to be the entire field of view of the PIV data. Explicit forms of Eq. (2.1) for both assumptions are presented by Gomez (2024), along with descriptions of the boundary conditions.

Equation (2.1) can be expressed as $(-i\omega + \mathcal{L})\hat{\mathbf{q}} = \hat{\mathbf{f}}$, where $\hat{\mathbf{q}} = [\hat{\mathbf{u}}, \hat{p}]$ and $[\hat{\mathbf{f}}_{\mathbf{u}}, 0]$. The resolvent operator \mathcal{R} is then defined as $\mathcal{R} = (-i\omega + \mathcal{L})^{-1}$ such that $\hat{\mathbf{q}} = \mathcal{R}\hat{\mathbf{f}}$. In resolvent analysis, one seeks the unit-norm forcing that leads to the largest response. Here, both the response and the forcing are measured through the norm induced by the kinetic energy inner product

$$\langle \mathbf{a}, \mathbf{b} \rangle = \int_V (a_u^* b_u + a_v^* b_v + a_w^* b_w) d\mathbf{x}_n = \mathbf{a}^* \mathcal{W} \mathbf{b}, \quad (2.3)$$

where the integration is over the entire subdomain where x_n is defined, \mathcal{W} is a positive-semi-definite operator, and $*$ denotes complex conjugate. Unlike the analysis presented by Gomez (2024), the biglobal resolvent analysis examined here does not use any masking in the domain. The unit-norm forcing input that leads to the largest amplification is the solution of the eigenvalue problem

$$\mathcal{R}^\dagger \mathcal{W} \mathcal{R} \phi_i = \sigma_i^2 \mathcal{W} \phi_i, \quad (2.4)$$

where \dagger denotes the adjoint operator. Since $\mathcal{R}^\dagger \mathcal{W} \mathcal{R}$ is positive semi-definite, σ_i^2 are guaranteed to be positive and the forcing modes, ϕ_i , are orthonormal with respect to the inner product in Eq. (2.3). The indices i are ordered such that $\sigma_i \geq \sigma_{i+1}$. The response modes, ψ_i , are defined as $\sigma_j \psi_i = \mathcal{R} \phi_i$. The set of ψ_i is also orthonormal with respect to the inner product in Eq. (2.3).

The inhomogeneous directions are discretized using fourth-order summation-by-parts differentiation schemes. For the local scheme, we use $N_y = 199$ points in the wall-normal direction. For the biglobal scheme, we use $N_x = 500$ points in x and $N_y = 301$ points in y . We use an Arnoldi algorithm to solve Eq. (2.4) and make use of lower-upper decompositions to avoid explicit storage and calculation of \mathcal{R} . See Gomez (2024) for additional details on the discretization and schemes for the solution of the eigenvalue problem.

In this study, we primarily focus on the optimal response, $\sigma_1 \psi_1$. To consider the

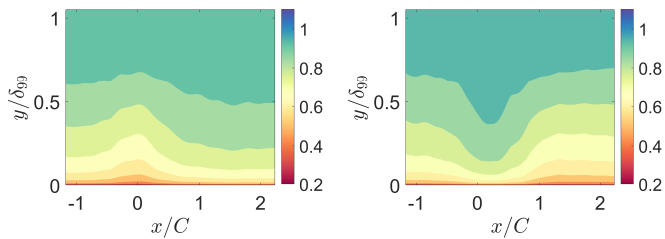


Figure 2: (a) AOA = 8° (FPG case) and (b) AOA = -8° (APG case). Normalised streamwise velocity contours U/U_e at $Re_\tau \approx 6000$. $x/C = 0$ represents airfoil leading edge.

amplification across all scales, we perform sweeps over the wavenumber and frequency space. We then plot the premultiplied amplification,

$$E_{u,1D}(y, \omega) = \omega \int \int \int |\sigma_1(k_x, k_z, \omega) \psi_{1,u}(y; k_x, k_z, \omega)|^2 dk_x dk_z, \quad (2.5)$$

$$E_{u,2D}(y, \omega) = \omega \int \int |\sigma_1(k_z, \omega) \psi_{1,u}(x_r, y; k_z, \omega)|^2 dk_z, \quad (2.6)$$

where $E_{u,1D}$ is performed for the local analysis and $E_{u,2D}$ for the biglobal analysis similar to Gomez (2024). Note that $E_{u,2D}$ compares the energy amplification of the mode at one specific location, x_r , which was chosen as the hot-wire location in the experiment to compare the linear response and the experimental measurements.

2.3. Details of the sweep

The 1D local resolvent sweep uses $84 k_x^+$ between $2\pi/10$ and $2\pi/(50Re_\tau)$ and $20 k_z^+$ between $2\pi/10$ and $2\pi/(5Re_\tau)$, both logarithmically spaced. Furthermore, the critical layer (y_c), defined as the wall-normal support for the most amplified velocity response (McKeon & Sharma 2010), for the sweep was restricted to between $2.6 \times Re_\tau$ and $0.5 \times Re_\tau$. The wave speed, C , is defined as the local mean velocity that is a function of y_c , and a sweep in frequency is performed by relating it to the streamwise wavenumber and wave speed, $\omega = C(y_c)k_x$.

The biglobal sweep uses $24 k_z^+$ between $2\pi/250$ and $2\pi/60000$ and $25 \omega^+$ between $2\pi/250$ and $2\pi/100000$, both logarithmically spaced. Since this study focuses on large-scale amplification, the spanwise wavenumbers and frequencies associated with small scales, such as those associated with the near-wall cycle, are not included in the sweep.

3. Results

Figure 2 shows the impact of the mean pressure gradient on the mean-velocity field. The contours show the streamwise velocity normalized by the local edge velocity. The x axis has been normalized by the length of the airfoil chord C , and $x/C = 0$ corresponds to the leading edge of the airfoil. In terms of boundary layer thickness, the size of our PIV domain extends beyond $26\delta_{99}$ in the streamwise direction. The y axis has been normalized by the local boundary layer thickness, as such growth of the boundary layer is not shown. For the AOA = 8° case, the flow experiences a slight deceleration in the streamwise direction close to the airfoil leading edge, followed by an acceleration of the flow in the streamwise direction afterward. In the remainder of this report, this case

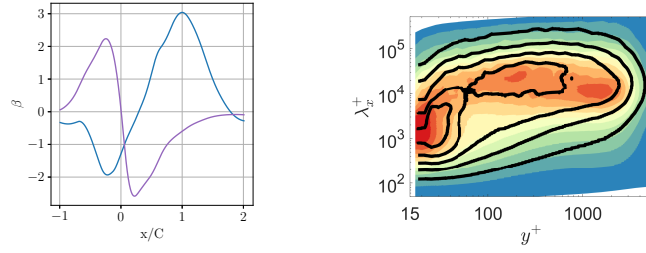


Figure 3: (a) Clauser's equilibrium parameter, β , as function of streamwise location. The solid blue line corresponds to the airfoil at -8° AOA, while solid purple lines are for AOA = 8° . (b) Premultiplied one-dimensional streamwise velocity energy spectra, measured at $x/C = 2$ (one chord downstream). Filled coloured contours correspond to the airfoil at -8° (APG case) while solid black contours are for AOA = 8° (FPG case)

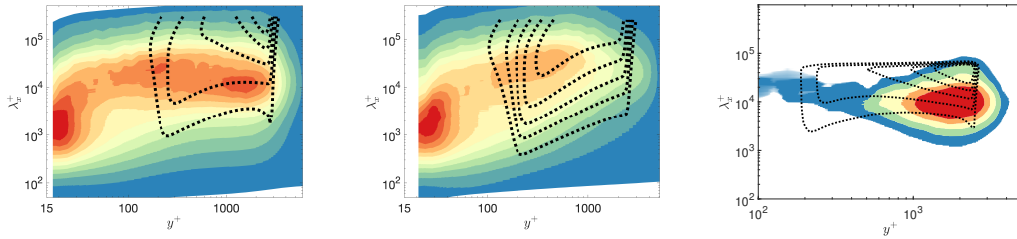


Figure 4: Premultiplied one-dimensional streamwise velocity energy spectra E_{uu}^+ , measured at $x/C = 2$ (one chord downstream) in filled colored contours and $E_{u,1D}^+$ plotted in dotted black contours. (a) AOA = -8° (APG case); (b) AOA = 8° (FPG case) and (c) Difference spectra. Note that contour levels are normalized by their maximum value, and each contour level is offset by 0.1.

is referred to as the FPG case. In contrast, for the case where the airfoil is placed at AOA = -8° , the mean flow gradient shrinks near the leading edge of the airfoil and grows subsequently. The AOA = -8° is referred to as the APG case. The impact of the mean-pressure gradient can also be quantified by Clauser's parameter, plotted in Figure 3. For the APG case, β becomes negative at the leading edge of the airfoil, before recovering to a maximum value of 3, close to the trailing edge of the airfoil. For the FPG case, the amplification in β occurs near the quarter-chord, where $\beta \approx 2.5$. These values of β , are much higher than any previous study (Sanmiguel Vila *et al.* 2020; Vishwanathan *et al.* 2023) performed at high Reynolds number in attached flows. For equilibrium flows with β remaining roughly constant (Clauser 1956), the rate at which pressure increases is counteracted by the local wall shear stress, producing self-similar velocity profiles. However, as shown in Figure 3(a), β is not constant in this study. However, β approaches zero both at the beginning and at the end of the PIV domain. Although β does reach zero one chord length downstream of the airfoil trailing edge, the flow still experiences different histories in the two cases plotted.

To acquire frequency-related information about the turbulent kinetic energy linked to streamwise velocity disturbances, the premultiplied streamwise energy spectral density, $E_{uu}(y, \kappa_x)$, is computed from HWA data for both APG and FPG cases. The HWA is positioned at $x/C \approx 2$, where the local value of $\beta \approx 0$, in the presence of APG and

FPG histories. Figure 3(b) plots the case with APG history in filled contours, while the contour lines represent the FPG case. In both cases, there is an inner peak at $y^+ \approx 15$, linked to the near-wall cycle. Furthermore, both cases show a secondary peak, which is linked to VLSMs (Hutchins & Marusic 2007), at $y^+ \approx 300$. The only visible difference in the estimated $E_{uu}(y, \kappa_x)$ is found farther away from the wall, at $y^+ \geq 1000$. While for the FPG history case, only the inner and outer peaks are visible, for the APG history case, an additional outer layer peak can be seen. In the remainder of this report, we to this peak as the pressure gradient peak. It is important to note that the decoupling of the VLSM peak ($y^+ \approx 300$) and the pressure gradient peak ($y^+ \approx 1000$) is possible only if Re_τ is sufficiently high (see Sanmiguel Vila *et al.* 2020, for instance). Furthermore, the wavelength of the pressure gradient peak, $(\lambda_x^+) \approx 9000$, is shorter than that of VLSM peak, which can extend up to $(\lambda_x^+) \approx 11000$. As such, Figure 3(a) shows that the impact of the pressure gradient upstream is retained at the downstream locations, where $\beta \approx 0$.

The $E_{uu}(y, \kappa_x)$, obtained from experiments (solid contours) is compared with the $E_{u,1D}$ computed from the local 1D resolvent analysis (line contours) for the APG and FPG cases in figures 4(a) and 4(b), respectively. As rank-1 amplification is used without weighting (broadband forcing), absolute levels cannot be compared. In the absence of absolute values for the integrated streamwise energy density from the resolvent analysis, a more meaningful result is obtained by taking the differences in streamwise energy density between the $AOA = -8^\circ$ and $AOA = 8^\circ$ cases, both performed at similar $Re_\tau \approx 6000$, shown in Figure 4(c). The resolvent analysis reveals amplification in the outer layer (over a range of wall-normal locations) that is comparable to that observed in measurements. However, the predicted streamwise wavelengths appear to be different from those observed in measurements, possibly because of the amplification from the critical layer mechanism. Measurements show that there are two distinct differences: intensification of VLSMs between the APG and FPG cases and the emergence of the second outer peak due to APG at a smaller length scale. The energetic wavelength in the resolvent analysis appears to be consistent with that of VLSMs across all wall-normal locations. If this reduction in wavelength observed in measurements is an effect of pressure gradient history, then, the local 1D analysis cannot capture it, as it does not include the history effects. However, if the differences between the FPG and APG cases can be interpreted as stemming from changes in the local mean that result from the different upstream pressure gradient histories, then some trends should be captured with the local analysis. It may be possible to interpret the differences observed in the resolvent analysis as an indirect manifestation of history effects that appear to affect only the VLSM scales. However, the fact that there is a difference between the local resolvent results and measurements suggests the need to capture the history effects more explicitly. This can be achieved only through a biglobal analysis where non-parallel effects can be included.

3.1. Biglobal resolvent analysis

Here, we apply biglobal resolvent analysis to analyze linear amplification in the TBL subject to complex pressure gradient histories. This allows us to incorporate nonparallel effects in the TBL, especially considering the different upstream histories. Figure 5(a) plots σ_1 across the wavelength $\lambda_z = 2\pi/k_z$ and period $\lambda_t = 2\pi/\omega$ used in the sweep. Both the FPG (on the left) and APG (on the right) cases identify the largest amplification for $(\lambda_z^+, \lambda_t^+) \approx (600, 600)$; however, the APG case has larger σ_1 than the FPG case. This points to amplification mechanisms that are present in the APG TBL that are mitigated in the FPG, which may also play a role in the energization of large-scale

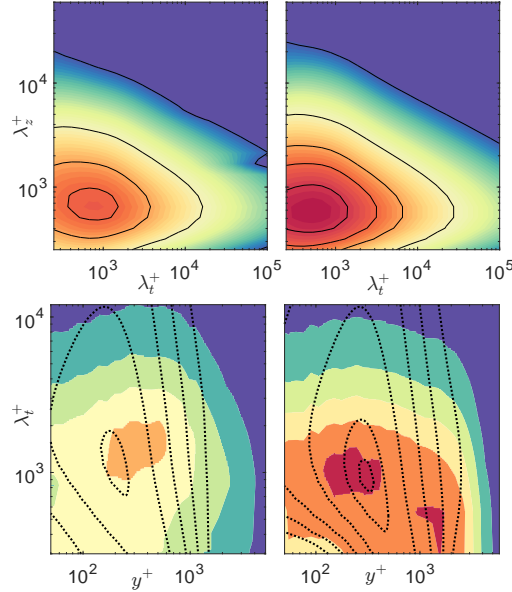


Figure 5: (a) Energy contained in the leading singular values, normalized with inner units, for different timescales and spanwise wavelengths obtained from resolvent analysis and (b) Premultiplied spectra ($E_{uu}(y, \lambda_t)$) from measurements (filled contours). Comparison of the FPG (left) and APG (right) cases.

turbulent structures in the experimental measurements. The increase in amplification due to an increase in the upstream β also agrees with similar results from Gomez (2024) for smaller Re_τ and is consistent with the energization of large scales observed in APG TBL simulations (Bobke *et al.* 2017). Note that the intensification of large scales is consistent with VLSM-type features, which is confirmed by examining the spanwise spectra of the wall-normal location where the most amplified spanwise length scale is associated with VLSM structures (not shown in Figure 5 for brevity). Overall, the biglobal analysis appears to capture the intensification of VLSM-type structures with changes in pressure gradient history.

Figure 5(b) compares the kinetic energy spectra ($E_{u,2D}$) from the biglobal resolvent analysis (in dashed lines) with those of the hot-wire measurements (in filled contours). Variations in timescales (λ_t^+) with normal wall location (y^+) are shown for the FPG case (on the left) and the APG case (on the right). Note that the comparison is done only over a limited range of wall-normal positions and timescales to highlight the similarities and differences in the spectra. $E_{u,2D}$ attains local maxima at $(\lambda_t^+, y^+) \approx (1000, 300)$ for both the APG and FPG cases. In comparison with the hot-wire measurements, the VLSM peak present in the experimental data appears to be captured by the biglobal resolvent analysis. This is consistent with the results from the local analysis; however, the exact wall-normal location of the energetic peaks is marginally different. The intensification of the VLSM peak by the APG flow is reflected by an increase in the amplification using the APG mean flow field compared with the results using the FPG. The APG measurements identify an outer-scaled peak associated with the APG. A reason for the increase in the amplification of the VLSM peak identified in the biglobal results could be that the APG case experiences increased mean shear relative to the FPG case. As shown in Figure

2, where the APG experiences increased shear upstream, where the flow is accelerated under the airfoil. This creates a region of increased shear that is not reflected in the FPG case and thus is a source of non normal amplification that is mitigated in the FPG mean flow field.

A distinct secondary peak is not identified in the contours of $E_{u,2D}$ from the resolvent analysis; however, there is more amplification in the APG than in the FPG in the outer region, probably due to the increased wake. Note that $E_{u,2D}$ looked only at the optimal modes, which are often concentrated closer to the wall than the sub optimal modes to take advantage of the mean shear amplification. Future work will take into account higher-order modes in the calculation of $E_{u,2D}$. Finally, in contrast to Gomez (2024), the biglobal analysis did not observe near-wall peaks, because the sweeps in k_z and ω were chosen to identify only large-scale modes. Because of the absence of small-scale modes in the sweep, masking is used to highlight the near-wall modes, further mitigating the amplification of the near-wall structures at the reference location.

4. Conclusions

This study examines the influence of pressure gradient histories on high Reynolds number TBLs. The experiments were carried out at the boundary layer wind tunnel facility at the University of Southampton. Measurements were performed in a large domain at $Re_\tau \approx 6000$, in flow over smooth walls subjected to FPGs and APGs. This was achieved by changing the angle of attack of a fixed 2D wing positioned above the boundary layer, which yielded positive and negative values of Clauser's equilibrium parameter β . As such, this study extends the state of the art by exploring flows at high Reynolds numbers with novel sets of measurements for non-equilibrium boundary layers. A low-order representation of this problem was obtained by applying a resolvent analysis to experimental mean flow data. In particular, the biglobal resolvent analysis was used to capture nonparallel flow effects, while a local resolvent analysis was performed at a downstream location where $\beta \approx 0$.

Although local resolvent analysis cannot provide an assessment of individual cases, the difference in energy between the APG and FPG cases can be inferred. It is primarily due to some aspects of pressure gradient history that are included in the local mean flow. The analysis indicates that most of the amplification is concentrated on VLSM-type scales across all wall-normal positions. Much better agreement is obtained using the biglobal analysis, which appears to amplify the VLSM scales at the appropriate wall-normal location. As such, modulation of the VLSM by the mean pressure gradient is partly a shear-driven phenomenon; therefore, it is encouraging that the resolvent analysis can capture this difference. However, the pressure gradient peak observed on a smaller length scale farther away from the wall in the measurements is not captured by the resolvent analysis. Further exploration of these differences, as well as the development of scaling relationships, will be necessary to gain more insights from the resolvent analysis. This will be a subject of future work in this area.

Acknowledgments

The authors acknowledge EPSRC, which funded the experimental work, the CTR summer program for enabling the modeling work, and Dr. Xiang Yang for his comments on this report.

REFERENCES

- AUBERTINE, C. D. & EATON, J. K. 2005 Turbulence development in a non-equilibrium turbulent boundary layer with mild adverse pressure gradient. *J. Fluid Mech.* **532**, 345–364.
- BLAKE, W. K. 2012 *Mechanics of Flow-Induced Sound and Vibration: General Concepts and Elementary Sources*. Elsevier.
- BOBKE, A., VINUESA, R., ÖRLÜ, R. & SCHLATTER, P. 2017 History effects and near equilibrium in adverse-pressure-gradient turbulent boundary layers. *J. Fluid Mech.* **820**, 667–692.
- CLAUSER, F. H. 1956 The turbulent boundary layer. *Adv. Appl. Mech.* **4**, 1–51.
- GOMEZ, S. R. 2024 Linear amplification in nonequilibrium turbulent boundary layers. PhD thesis, California Institute of Technology.
- HARUN, Z., MONTY, J. P. & MARUSIC, I. 2011 The structure of zero, favorable and adverse pressure gradient turbulent boundary layers. *In Proceedings of the 7th International Symposium on Turbulence and Shear Flow Phenomena 2011-July*, 1–6.
- HARUN, Z., MONTY, J. P., MATHIS, R. & MARUSIC, I. 2013 Pressure gradient effects on the large-scale structure of turbulent boundary layers. *J. Fluid Mech.* **715**, 477–498.
- HUTCHINS, N. & MARUSIC, I. 2007 Evidence of very long meandering features in the logarithmic region of turbulent boundary layers. *J. Fluid Mech.* **579**, 1–28.
- MCKEON, B. J. & SHARMA, A. S. 2010 A critical-layer framework for turbulent pipe flow. *J. Fluid Mech.* **658**, 336–382.
- MOARREF, R., SHARMA, A. S., TROPP, J. A. & MCKEON, B. J. 2013 Model-based scaling of the streamwise energy density in high-Reynolds-number turbulent channels. *J. Fluid Mech.* **734**, 275–316.
- SANMIGUEL VILA, C., VINUESA, R., DISCETTI, S., IANIRO, A., SCHLATTER, P. & ÖRLÜ, R. 2020 Separating adverse-pressure-gradient and Reynolds-number effects in turbulent boundary layers. *Physical Review Fluids* **5**, 064609.
- TANNER, L. & BLOWS, L. 1976 A study of the motion of oil films on surfaces in air flow, with application to the measurement of skin friction. *J. Phys. E Sci. Instrum.* **9**, 194.
- VISHWANATHAN, V., FRITSCH, D. J., LOWE, K. T. & DEVENPORT, W. J. 2023 History effects and wall-similarity of non-equilibrium turbulent boundary layers in varying pressure gradient over rough and smooth surfaces. *Int. J. of Heat and Fluid Flow.* **102**, 109145.
- VOLINO, R. J. 2020 Turbulence structure in non-equilibrium boundary layers with favorable and adverse pressure gradients. *Int. J. of Heat and Fluid Flow.* **86**, 108717.